buildings

MDPI

Article

Mechanical Properties and Microstructure Analysis of Cement Mortar Mixed with Iron Ore Tailings

Junsheng Li [1], Wenyuan Ren [1,*], Aijun Zhang [1], Shuangcun Li [1], Jianping Tan [1] and Hongtai Liu [2]

[1] College of Water Resources and Architectural Engineering, Northwest A&F University, Yangling 712100, China
[2] China Jikan Research Institute of Engineering Investigations and Design Co., Ltd., Xi'an 710000, China
* Correspondence: wenyuange304@nwafu.edu.cn

Abstract: In order to study the feasibility and sand substitution mechanism of cement mortar mixed with iron ore tailings (IOT), iron ore tailings cement mortars (referred to as IOTC) with IOT content of 0%, 25%, and 50% were made and tested. First, the basic properties of IOT used were measured to verify the theoretical feasibility. Second, the uniaxial compressive and tensile strengths, as well as the crack resistance performance of IOTC under different curing ages and different sand substitution rates were tested. Third, the techniques of inductively coupled plasma atomic emission spectrometry (ICP-OES), X-ray diffraction (XRD), nuclear magnetic resonance (NMR), scanning electron microscopy and energy-dispersive spectroscopy (SEM-EDS) were used to study the influence of curing age and different sand substitution rates on the chemical, mineralogical, and microstructural characteristics of IOTC. The sand substitution mechanism of IOT was then discussed. The research results proved the feasibility of using IOT to substitute standard sand in cement mortar. Within substitution rate of 0–50%, the mechanical properties increased with the increase of substitution rate. Though limited chemical effects were found by adding IOT, in comparison with standard sand mortar, more hydration products were found and the pore size distribution was changed for IOTC, which corresponds to its mechanical improvement.

Keywords: cement mortar; iron ore tailings; solid waste utilization; mechanical properties; microstructure

Citation: Li, J.; Ren, W.; Zhang, A.; Li, S.; Tan, J.; Liu, H. Mechanical Properties and Microstructure Analysis of Cement Mortar Mixed with Iron Ore Tailings. *Buildings* **2023**, *13*, 149. https://doi.org/10.3390/buildings13010149

Academic Editor: Shazim Memon

Received: 26 October 2022
Revised: 22 December 2022
Accepted: 3 January 2023
Published: 6 January 2023

1. Introduction

The implementation of China's national carbon peaking and carbon neutrality goal has made the clean utilization of secondary resources and metallurgical waste an urgent need. Tailings are the largest source of waste after metallurgical beneficiation and extraction [1,2], of which iron ore tailings (IOT) account for the biggest proportion [3,4]. Due to the lack of effective treatment, the accumulation of IOT not only occupies a lot of land resources, but also pollutes the environment. At present, the following methods are mainly used to comprehensively recycle tailings [5,6]: backfilling in mines with lower performance requirements; using as raw materials for various building materials; or further recycling of valuable metals. However, how to improve the utilization rate of IOT is still a big challenge.

Concrete and cement mortar are important building materials in the engineering field, and natural river sand or machine-made sand are important raw materials. The reserves of natural river sand are depleted due to long-term exploitation, and machine-made sand is more suitable for small-scale laboratory use due to its high cost. Therefore, it is also urgent to find alternative sources of sand [7,8].

The main components and physical forms of IOT sand are similar to those of machine-made sand, and it has the potential to replace river sand [9–11], which can not only reduce production costs, but also realize the waste utilization of IOT. In recent years, great progress has been made in this field. IOT sand was first used by Huang et al. [12] as a mortar fine aggregate to make iron ore tailings cement mortar (IOTC), and researchers compared its

performance with natural sand cement mortar, confirming the availability of using IOT to replace natural sand as a fine aggregate. It is proved that the high strength of IOT itself as a skeleton improves the mechanical properties of the mortar. Siddique et al. [13] concluded that the addition of a small amount of tailings sand (10%) could fill the micropores to reduce the internal porosity of the cement mortar, and the durability of the cement mortar was also improved. In addition, the potentially active substances in IOT undergo secondary hydration under alkaline conditions, reacting with calcium hydroxide to form calcium silicate hydrate (C-S-H), which causes the internal structure of the mortar to be more compact and improves its mechanical strength. Wu and Liu [14] used scanning electron microscopy (SEM) to observe the microscopic morphology of IOTC. Zhang et al. [15] captured the morphology and element changes of the aggregate-matrix interface between IOT sand and natural sand in different gel materials, confirming the "volcanic ash effect" of IOT.

The feasibility of replacing natural river sand with IOT to make cement mortar has been confirmed in the literature [16–18]. Due to the multi-angle and high micro powder content of IOT sand, the fluidity of the mortar will be affected, but its strength will not be weakened. At present, most research focuses on the influence of IOT sand content on the basic mechanical properties of concrete and cement mortar [19,20]. There are few in-depth studies on the sand substitution mechanism of tailings, or comprehensive analyses of the mechanism of internal active hydration products and inert pore size distribution.

For the sake of description, the secondary reaction between the active material in the IOT and the cement hydration products, as well as the enhancement of the cement hydration reaction, are referred to as the "chemical effects" of IOT. The "chemical effects" vary over time. Second, the filling effect, micro-aggregate effect, and water reduction effect of tailings and inert materials are called the "physical effects," which do not change over time, but are determined by the tailings mix.

In this study, based on the results of existing studies, the IOT sand from Shangluo, Shaanxi Province, China, is used. Firstly, its basic properties are analyzed to verify the theoretical feasibility of it replacing standard sand in cement mortar. Secondly, mortar specimens with different curing ages of 3 d, 7 d, 28 d, 120 d and sand substitution rates of 0%, 25%, and 50% were prepared. The effects of sand substitution rate and curing age on the mechanical properties, such as uniaxial compressive strength uniaxial tensile strength, and crack resistance performance were analyzed to confirm the feasibility of IOT sand substitution. The changes of internal hydration products and their relative contents at different curing ages after incorporating IOT tailings were analyzed to explore the "chemical effects". The "physical effects" with regard to the internal pore structure of IOTC were also discussed. The research results provide potential references for engineering project cost reduction and tailings solid waste utilization.

2. Materials and Test Methods

2.1. Materials

(1) Fine aggregate. The machine-made standard sand (Xiamen ISO Standard Sand Company Limited, Xiamen, China) was used, including three gradations: coarse sand, 1.0–2.0 mm; medium sand, 0.5–1.0 mm; and fine sand, 0.08–0.5 mm. A full bag of standard sand is about 1350 g, with each gradation comprising 450 g. Additionally, the whole bag was used to ensure that the standard gradation remained unchanged during preparation. The IOT sand used in the test was from iron tailings in Zhashui County, Shangluo City, Shaanxi Province. The IOT sand was yellowish-brown in color, and had rough surfaces with many edges and corners.

(2) Cement. The P·O 42.5 ordinary cement (Jidong Cement Company Tangshan, China) was used, which has compressive strengths of 30.5 MPa and 59.1 MPa, and flexural strengths of 4.8 MPa and 8.6 MPa for 3d and 28d curing ages (provided by the Jidong Cement Company), respectively.

(3) Water. Laboratory tap water was used.

(4) The water–cement ratio was 0.45, and the cement–sand ratio was 1:3. According to China Specification GB/T 17671-1999 [21], the mix ratio of different compositions is shown in Table 1. The samples of CM, IM1, and IM2 correspond to the sand substitution rates of 0%, 25%, and 50%, respectively. Prefixes of T, S, W, and O correspond to different curing ages of 3 d, 7 d, 28 d and 120 d respectively. For example, SIM1 represents the mortar sample with a curing age of seven days and a 25% sand substitution rate.

Table 1. Mix ratio of cement mortar with different compositions, kg/m^3.

Sample	Water	Cement	Sand	Tailings	Substitution Rate	Flow Value (mm)
CM	205	455.56	1366.67	0.00	0%	210
IM1	205	455.56	1025.00	341.27	25%	185
IM2	205	455.56	683.33	683.33	50%	160

Rate means IOT replacement rate.

2.2. Test Methods

The experimental investigations include mechanical, chemical, mineralogical, and microstructural tests. Mechanical tests include a uniaxial compressive test, uniaxial tensile test, and fracture test.

The chemical test uses inductively coupled plasma atomic emission spectrometry (ICP-OES). The mineralogical test is X-ray diffraction (XRD), and the microstructural tests use nuclear magnetic resonance (NMR) and scanning electron microscopy and energy-dispersive X-ray spectroscopy (SEM-EDS). To analyze the "chemical effects", the ICP-OES test can be used to infer the internal chemical reactivity of the specimens. Combined with XRD results, this can demonstrate the effect of tailings incorporation on the internal chemical reactivity of the mortar. NMR and SEM results can be used to obtain the internal pore and microstructure changes of the mortar to analyze the "physical effects", so as to explore the mechanism of tailings substitution for sand and to get a full response to the change in mechanical properties.

2.2.1. Mechanical Tests

The uniaxial compressive test and uniaxial tensile test of the mortar specimen were carried out following the Chinese standard "Test code for hydraulic concrete" (SL/T352-2020) [22]. The compressive test specimen was a cube specimen with a side length of 70.7 mm. The tensile test specimen was prepared in an 8-shaped mold, as shown in Figure 1a, where A = 22.2 mm, B = 52.0 mm, C = 78.0 mm, D = 22.5 mm, and E = 0.5 mm. According to the recommendations of the International Society of Rock Mechanics [23], the semicircular bend (SCB, Figure 1b) test was used to determine crack resistance performance of mortar specimens, with radius R = 25 mm, thickness t = 20 mm, span length S = R = 25 mm, and slit width a = 0.4R = 10 mm. All samples were tested after the curing ages of 3 d, 7 d, 28 d, and 120 d with the curing conditions [22] of temperature at 20 °C ± 1 °C, and relative humidity of 90%.

2.2.2. IOT Characteristics

X-ray fluorescence spectrometry (XRF) was used to identify the chemical composition of the IOT, by using Axios (PANalytical, Netherlands). A Mastersizer 2000E laser particle sizer (Malvern, Malvern, UK) was used to measure the particle size and gradation distributions of the IOT tailings, and the test conditions were test range of 0.02–2000 μm, scanning rate of 1000 times/second, measuring time of 1 sample / 5 min.

The clay content of the IOT had been tested by the steps outlined in Figure 2 and Formula (1), and the density of the IOT had been tested according to the China Specification GB/T 14684-2022 [24].

$$Q_a = \frac{G_o - G_1}{G_0} \times 100 \quad (1)$$

where Q_a is the clay content of the sample (%); G_0 is the mass of the specimen dried before the test (g); G_1 is the mass of the specimen dried after the test.

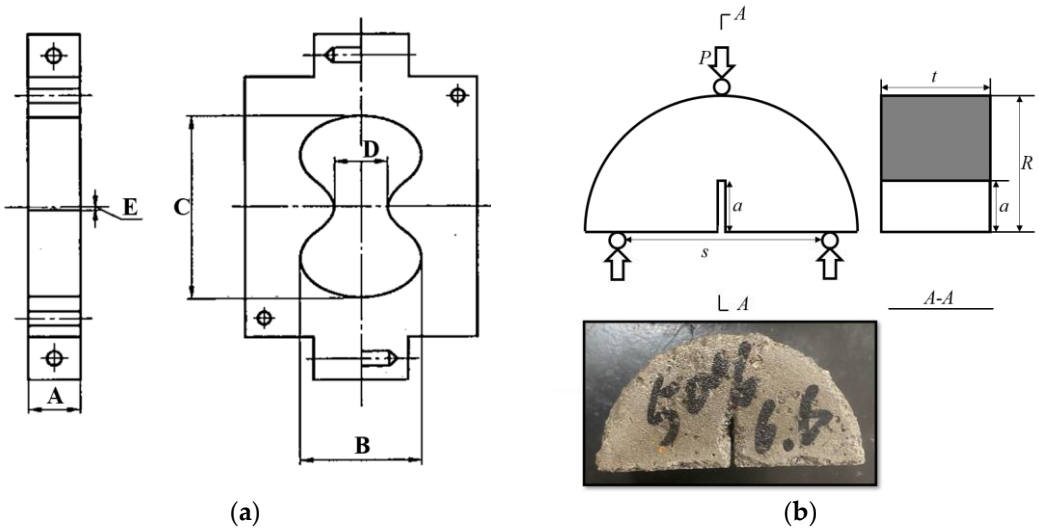

(**a**) (**b**)

Figure 1. (**a**) the 8-shaped mold; (**b**) semicircular bend specimen.

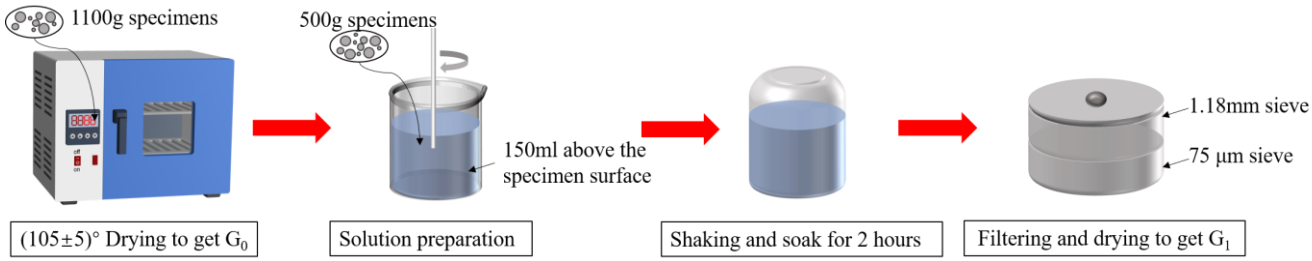

Figure 2. Clay content testing.

The flow value of IOTC was tested according to the GB/T 2419-2005 by using flow table [25]. The average of three measurements was used for determination of flow values.

2.2.3. Inductively Coupled Plasma Atomic Emission Spectrometer (ICP-OES)

The ion leachate from mortar specimens with different IOT mixtures at different curing ages was tested and analyzed by an inductively coupled plasma atomic emission spectrometer (ICP-OES) from ARCOS (Spectroscout, Kleve, German) to study the chemical interaction of IOT and the cement hydration products.

The samples were prepared by knocking and grinding the specimens from previous mechanical tests. According to the Chinese "Standard for Geotechnical Test Methods" (GB/T50123-2019) [26], 60 g specimens were mixed with 300 g of deionized water to make various types of specimen leaching solutions. The detailed flow chart is shown in Figure 3.

2.2.4. X-ray Diffraction (XRD)

A D8 ADVANCE A25 X-ray diffractometer (Bruker, Billerica, MA, USA) with CuKa radiation (40 mA and 40 KV) was used to analyze the internal components of mortar with different IOT at 7 d and 28 d. The samples were soaked in anhydrous ethanol for three days to stop the hydration and were dried at 60 °C for 1 h; then, the samples were crushed and ground, and passed through a 74 μm sieve. An appropriate amount of sample was placed on a slide, flattened, and compacted. Data were collected in 0.02° steps at a scanning speed of 5° per minute and a scanning range of 5 to 80°. The software jade6.5 (MDI Corporation, California, USA) was used for phase identification.

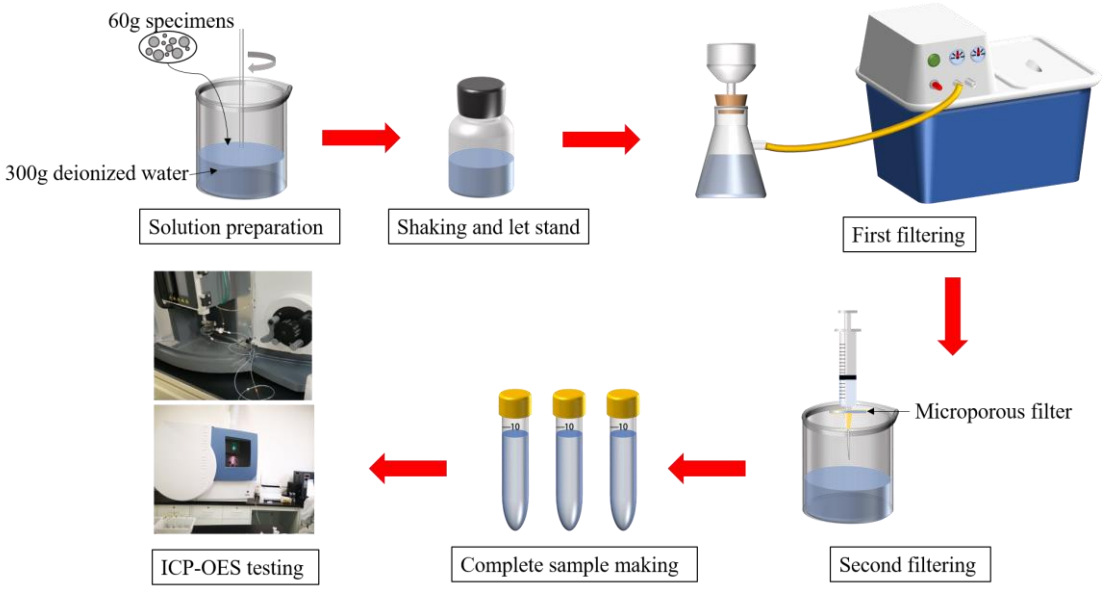

Figure 3. ICP-OES testing.

2.2.5. Nuclear Magnetic Resonance (NMR)

Cylindrical φ50 mm × 50 mm specimens with different IOT at 7 d and 28 d were prepared. The principle of the NMR test is to collect the pore water signal inside the specimen. Thus, the mortar specimens need to be vacuum saturated before testing. A MacroMR12-110V-I NMR analyzer (Niumag, Suzhou, China) from the Water Engineering Safety Research Center of Northwest Agriculture and Forestry University was used.

2.2.6. Scanning Electron Microscopy and Energy-Dispersive Spectroscopy (SEM-EDS)

Specimens with different dosing levels were tested after 7 d and 28 d of curing age using a Zeiss Sigma 300 scanning electron microscope (Zeiss, Oberkochen, German). The specimens were selected from the crushed material with diameter d $\leq$ 5 mm and thickness t $\leq$ 5 mm after mechanical tests, and directly glued to the test bench with conductive adhesive after vacuum gold coating to observe the internal morphology and microstructure of the mortar. The internal elemental contents were tested using the accompanying Energy-Dispersive X-ray Spectroscopy (EDS). Spot scans were performed for each of these samples for four times.

3. Results and Analysis

3.1. IOT Analysis

The results of the ICP-OES ion analysis are shown in Table 2, in which the ion content units are ppb and ppm, where ppm is equal to mg/mL, and ppb is one-thousandth of ppm. We mainly focused on ppm level elements, such as Mg, Ca, K, S, and Na. According to the ion detection results, the content of heavy metals in IOT was very low. This content is not high enough to cause harm to the environment or to human health, and would not have a significant impact on the use function of mortar. At the same time, it provides a reference for the phase analysis of IOT that follows below.

Table 2. ICP-OES ion analysis results.

Element		**Mg**	**Ca**	**K**	**S**	**Na**	**Fe**	**Mn**	**Zn**	**Cu**	**B**	**Al**
Content	Unit	ppm	ppm	ppm	ppm	ppm	ppb	ppb	ppb	ppb	ppb	ppb
	Value	14.7	7	168	24.7	2.496	145	132	57.5	10.7	860	82.19

The obtained XRD patterns are shown in Figure 4. From Figure 4, it can be seen that the main material components of iron tailings are quartz (SiO_2), calcite ($CaCO_3$), hematite (Fe_2O_3), and albite ($NaAlSi_3O_8$). The chemical composition of IOT determined by XRD and the chemical composition of the ISO sand provided by the manufacturer are shown in Table 3. The physical parameters of IOT and ISO sand are shown in Table 4; all the parameters of ISO sand are provided by the manufacturer, and the parameters of IOT sand had been tested.

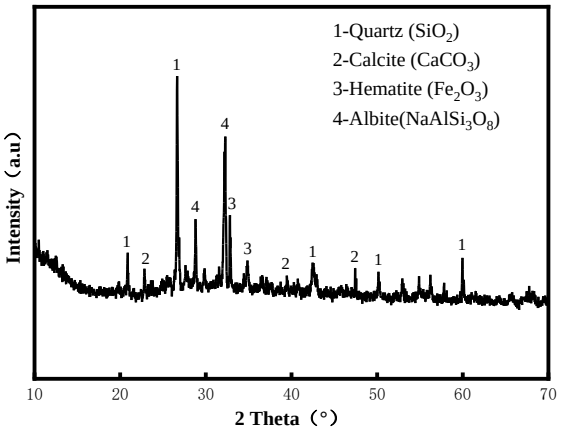

Figure 4. XRD patterns of IOT.

Table 3. Chemical composition of IOT and ISO sand (unit: %).

	SiO_2	Fe_2O_3	Al_2O_3	CaO	MgO	K_2O	Na_2O	SO_3	MnO_2	LOI
IOT	59.3	12.86	11.93	4.95	4.3	2.34	1.21	0.58	0.34	2.14
ISO sand	>96	<0.2	<0.2	<0.2	<0.2	<0.2	<0.2	<0.2	<0.2	<0.4

Table 4. Physical parameters of IOT and ISO sand.

	Apparent Density (kg/m^3)	Bulk Density (kg/m^3)	Clay Content (%)
ISO sand	2630	1480	<0.2
IOT	3110	1590	1.2

Particle size gradation: The sieve curves of IOT sand and standard sand are shown in Figure 5. The ISO standard sand is within the curve range of gradation zone II, and the IOT sand is within the curve range of gradation zone III. Figure 6 shows the particle size gradation curve of IOT sand [24].

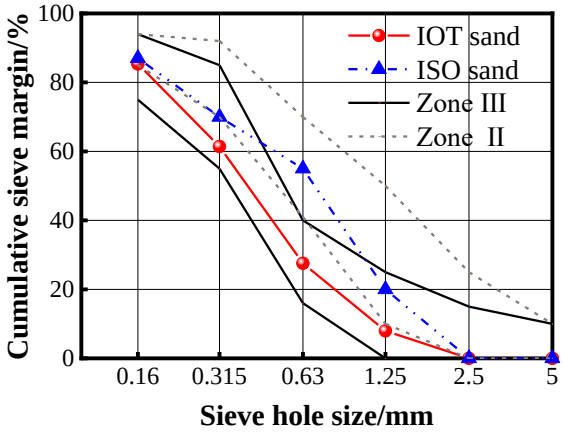

Figure 5. Sieve margin curve of IOT sand and ISO sand.

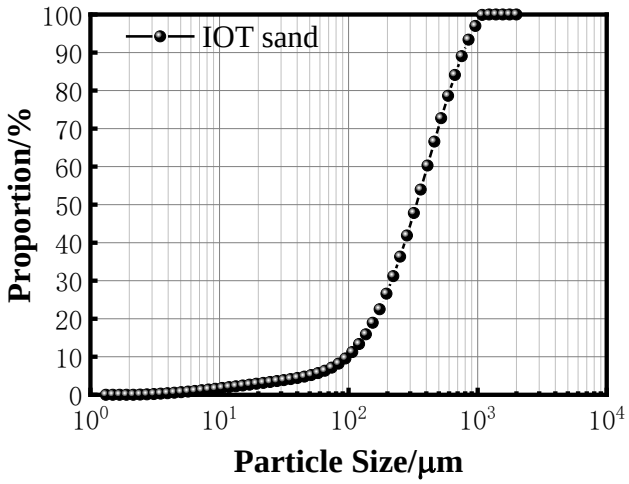

Figure 6. Particle size curve of IOT sand.

Combined with the above results, the fineness modulus μ_f of the IOT sand is 1.81, similar to the fine sand used in construction sand. Thus, it can be used as a fine aggregate to replace a portion of the ISO standard sand as a construction material.

3.2. Mechanical Tests

3.2.1. Mechanical Tests Analysis

All mechanical tests were performed on a microcomputer-controlled electronic universal testing machine, in which the uniaxial tensile test was loaded with a displacement control of 0.2 mm/min; the SCB three-point bending test was loaded with a displacement of 0.05 mm/min, and the uniaxial compression test was loaded with a load control of 0.3 MPa/s. The load and loading curves of the specimens at fracture were recorded, and the corresponding tensile and compressive strengths and ultimate fracture loads were calculated. Figure 7a–c shows the mechanical test results of each test specimen, and Figure 7d shows the comparison of the compressive strength at 28d with the results obtained by other authors.

It can be seen from Figure 7a–c that at the early ages (3 d, 7 d), the compressive strength (f_c), tensile strength (f_t), and ultimate fracture load (P_{max}) of the specimens all decreased slightly after adding tailings, but when the curing age was increased, the f_c, f_t, and P_{max} of the specimens increased rapidly; when the age reached 28 d and 120 d, the f_c, f_t, and P_{max} of the specimens all increased with the increase in the tailings substitution rate.

As can be seen in Figure 7d, similar conclusions have been obtained by other authors [20,27]. The use of iron tailings when replacing the aggregates of the mortar resulted in an enhancement of the compressive strength of the specimens at 28 d, and the enhancement increased after increasing the adding of IOT. It is worth mentioning that the difference in strength between these authors is caused by the different materials used but the trend is similar.

3.2.2. The Strength Activity Index a

The strength activity index a is used for the indirect analysis of the hydration activity of IOT incorporation, which is defined as follows [28,29]:

$$\alpha = \frac{f}{f_{0\%}} \text{ or } \alpha = \frac{P}{P_{0\%}} \quad (2)$$

where f and P are the strength values corresponding to a certain age after mixing with tailings, while $f_{0\%}$ and $P_{0\%}$ are the strength values corresponding to the specimens that remain unmixed with tailings at the same age.

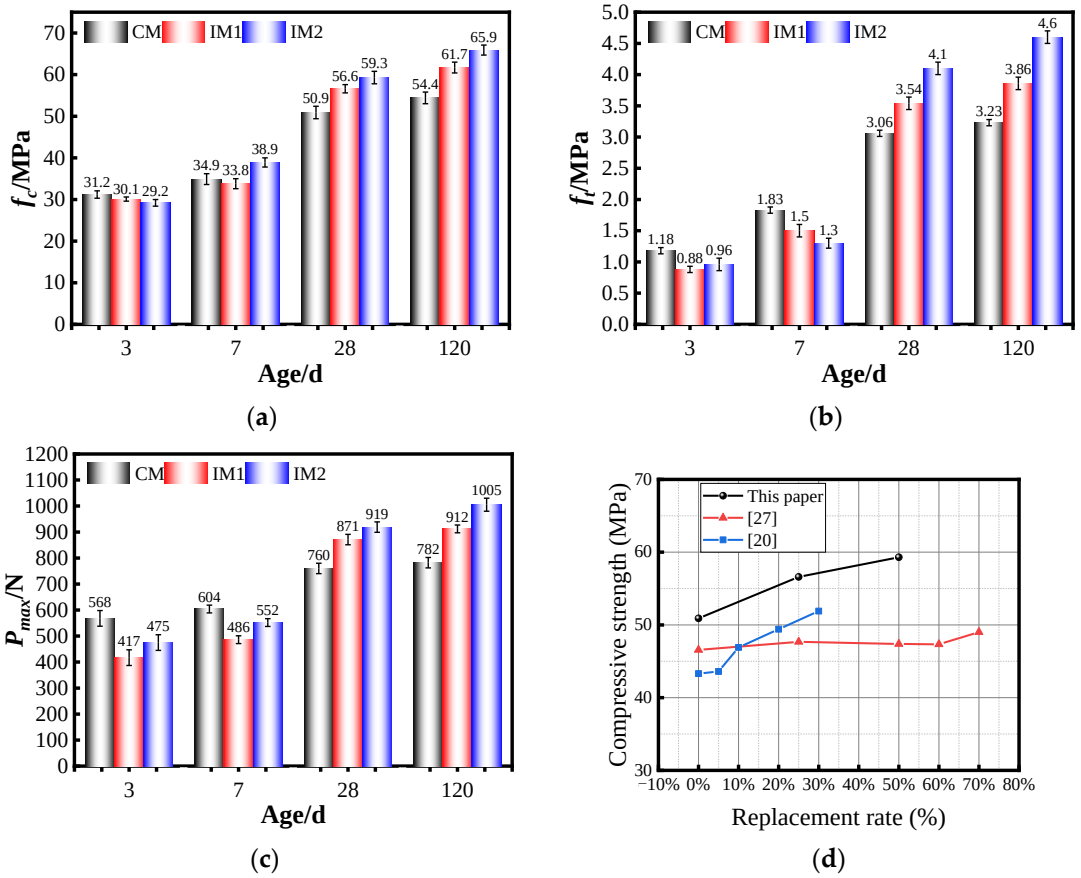

Figure 7. Mechanical test results of mortar with different ages: (**a**) uniaxial compressive strength; (**b**) uniaxial tensile strength; (**c**) ultimate fracture loads of SCB specimens; (**d**) comparison of compressive strength at 28 d.

Figure 8 shows the compressive strength activity index a_c, tensile strength activity index a_t, and cracking resistance activity index a_F. Larger values indicate higher activity of the tailings in the corresponding mechanical properties. It can be seen from Figure 8 that the strength activity indices at the standard age of 28 d and the late age of 120 d are higher than those at the early age (3 d and 7 d), while the strength activity indices at 28 d and 120 d increase as the amount of tailings in the admixture increases, indicating that more iron tailings are beneficial at later ages from the perspective of the mechanical strength activity index alone, as is also seen in other works [30–32].

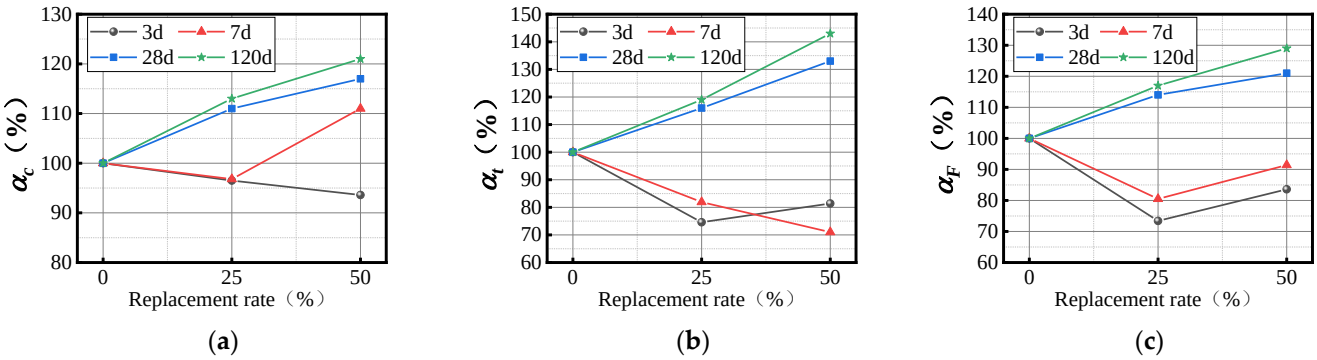

Figure 8. Strength activity index a of samples: (**a**) the compressive strength activity index a_c; (**b**) the tensile strength activity index a_t; (**c**) the cracking resistance activity index a_F.

3.2.3. The Strength Development Coefficient Index β

In addition, the strength development coefficient β is defined as the ratio of the mechanical strength of each type of specimen at different ages to its corresponding strength at 28 d [33]. It can be used to study the mechanical strength of different specimens according to the curing age history. By definition, before the age of 28 d, $\beta < 1$; a smaller β indicates more obvious growth in strength from this age to the standard age. After the age of 28 d, $\beta > 1$; a larger β indicates more obvious growth in strength after the standard age. Figure 9 shows the mechanical strength development coefficients for each type of specimen: β_c, β_t, and β_F are compressive strength development coefficient, tensile strength development coefficient, and cracking resistance development coefficient, respectively.

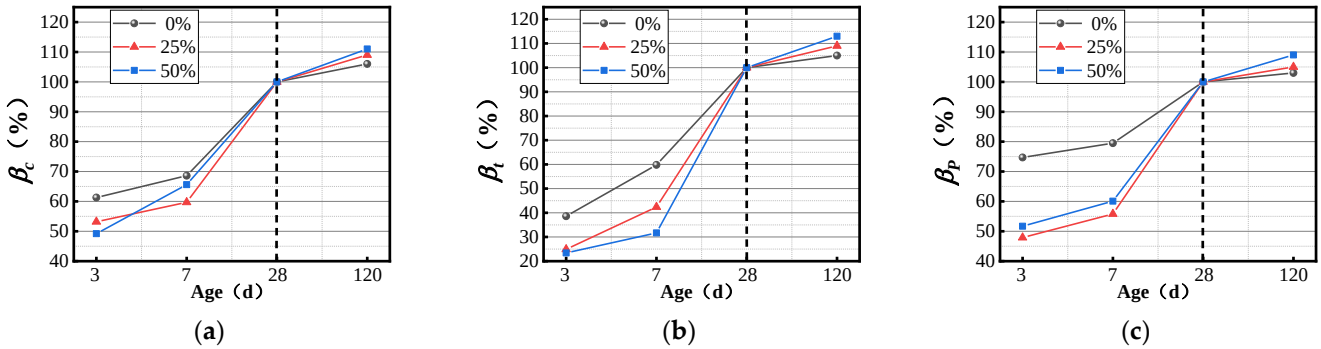

Figure 9. Development coefficient of strength for each category: (**a**) β_c; (**b**) β_t; (**c**) β_F.

From Figure 9, it can be seen that the β of all types of specimens after tailings incorporation are smaller than the β of specimens without tailings incorporation at the early stages (3 d, 7 d). There is an opposite trend (greater strength development for IOTC) for the curing age of 120 d, and the magnitude increases with the increase of IOT incorporation. In Figure 9a, the β_c for the 50% iron tailings mix is smaller at three days, while the β_c for the 25% iron tailings mix is smaller at seven days, and they are all smaller than those of specimens without tailings at the same age. At 120 days, the β_c for the 50% iron tailings mix is larger than that for the 25% mix. In Figure 9b, we can notice that β_t decreases with the increase of IOT incorporation at early ages (3 d, 7 d), and for the 50% admixture at 120 d curing age it reaches its highest value of 112%. In Figure 9c, the β_F corresponding to 25% tailings admixture at early age reaches the minimum value, and β_F corresponding to 50% at 120 d age obtains the maximum value. This indicates that the incorporation of IOT in the early stage of hydration will reduce the mechanical properties of the specimens, but can improve the growth capacity of the corresponding properties. At the early ages, this growth capacity is not positively correlated with the quantity of tailings incorporation, while after the standard age of 28 d, increasing the quantity of tailings will be more conducive to the development of strength.

In summary, before the 28d of curing age, the optimal quantity of IOT incorporation should be between 25–50%. In this interval, IOT can optimize aggregate gradation [34,35]. In addition, the optimal quantity of tailings is also related to the mechanical test type and sample size. With the increase of curing age, increasing IOT incorporation will further improve the hydration activity index (a) and mechanical performance improvement capacity (β).

3.3. Chemical, Mineralogical, and Microstructural Tests

3.3.1. Chemical Test

In order to study the internal chemical reactivity of the cement mortar after the adding of IOT, IOTC samples with a sand replacement rate of 0%, 25%, and 50% were cured at different ages: 3 d, 7 d, and 28 d, respectively. The ICP-OES ion analysis test was conducted

to obtain the concentration changes of the main ions (Ca^{2+}, K^+, Al^{3+}, Si^{4+}), as shown in Figure 10.

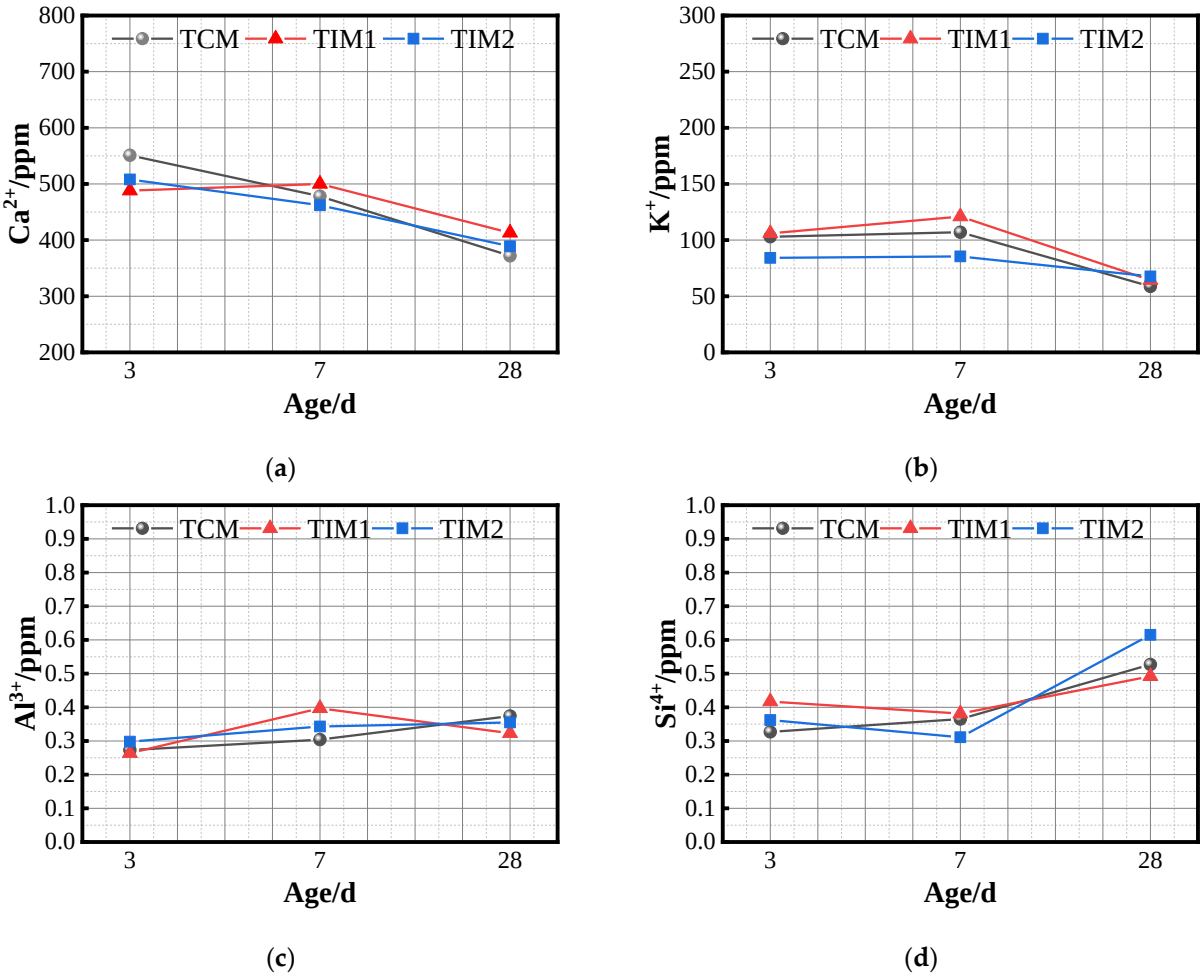

Figure 10. The concentration changes of the main ions: (**a**) Ca^{2+}; (**b**) K^+; (**c**) Al^{3+}; (**d**) Si^{4+}.

From Figure 10, the concentrations of free-state Ca^{2+} and K^+ ions are higher, while the concentrations of Al^{3+} and Si^{4+} ions are lower. The ions of Ca^{2+} and K^+ decrease with the increase of curing age, and the main reason may the decrease in the concentration of internal free-state ions caused by the precipitation of more hydration products. For Ca^{2+}, the incorporation of IOT had less influence on the trend of its content according to curing age, and Al^{3+} ions and Si^{4+} also showed a similar pattern. Thus, IOT without any treatment has limited influence on the chemical reactions inside the cement mortar. When a given content of ISO sand was replaced by IOT, the hydration reaction inside the mortar was not significantly changed.

3.3.2. Mineralogical Test

To further investigate the "chemical effect" of IOT incorporation on the internal chemical reactivity of mortar, an analysis was carried out from the perspective of physical phase transition. After 7 d and 28 d of curing ages, XRD tests were conducted. The XRD patterns are shown in Figure 11, and Table 5 shows the peak intensity of the main phases of each mortar sample.

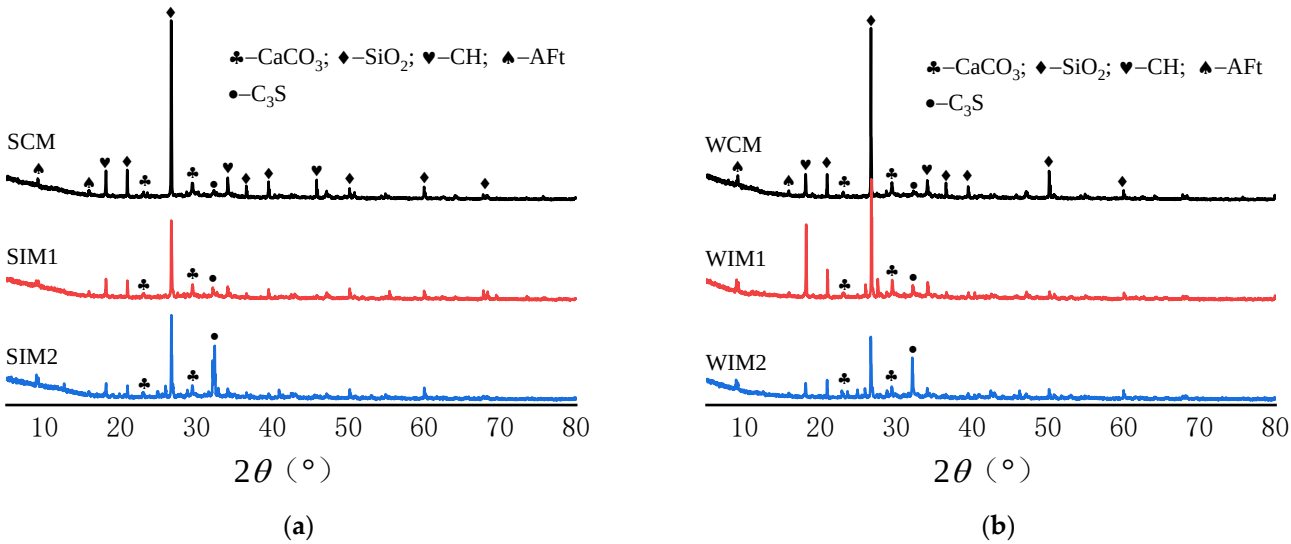

Figure 11. XRD patterns of different specimens: (**a**) 7 d; (**b**) 28 d.

Table 5. Peak intensity of the main peak phase of each mortar sample.

	AFt		$Ca(OH)_2$		$CaCO_3$		C_3S	SiO_2
Sample	**9.1°**	**15.5°**	**18.1°**	**34.2°**	**23.1°**	**29.4°**	**32.1°**	**26.7°**
SCM	574	301	782	609	264	481	300	4491
SIM1	592	311	613	423	258	476	401	2218
SIM2	672	333	535	405	312	485	1461	2052
WCM	622	298	705	552	265	496	295	4310
WIM1	595	279	1956	534	269	589	459	3077
WIM2	749	299	542	499	357	456	1167	1682

It can be seen from Figure 11 that the main phases in the mortar samples of various ages and different substitution rates are calcite ($CaCO_3$), silicon dioxide (SiO_2), portlandite ($Ca(OH)_2$), ettringite (AFt), and alite(C_3S);

In Table 5, the phase of C_3S is the main component of cement clinker and plays an important role in the early hydration of cement. At the same age, the intensity of C_3S diffraction peaks tends to increase with the increase of added IOT, while the highest diffraction peak of SiO_2 tends to decrease with the admixture of tailings. AFt, $Ca(OH)_2$, and $CaCO_3$ are the main components of cement hydration products, and the relative content of hydration products can be indirectly determined by their peak strengths [36–38]. Numerous research studies have concluded that AFt and $CaCO_3$ have a significant influence on the mechanical behavior of cement and cement mortar [39–41]. For the diffraction peak at 9.1°, tailings incorporation and longer curing age enhance AFt's diffraction peak intensity, with the highest peak of WIM1 reaching 749, but the overall variation is insignificant. Similarly, there is no significant change in the peak intensity of AFt in the diffraction peaks corresponding to 15.5° and 23.1°.

The variation of the diffraction peak intensity of $CaCO_3$ also shows a similar pattern to AFt, with a small overall variation, and the highest value of 589 for the WIM1 group. The phase of $Ca(OH)_2$ in cement is a hydration product of cement, with laminar results and lamellar morphology, which contributes less to the strength and may also be the origin of cracks when stressed. The intensity of $Ca(OH)_2$ diffraction peaks is shown in Table 5, which shows that it decreases significantly with the increase of IOT incorporation and curing age (except for the mutation in WIM1).

In summary, the XRD results are consistent with the results of the ion concentration analysis. The incorporation of tailings slightly enhances the hydration reaction, and the

peak intensity of the diffraction peaks of the main hydration products such as $Ca(OH)_2$, AFt, and $CaCO_3$ are slightly increased. However, the overall change is very small, and the incorporation of IOT does not significantly increase the hydration. The chemical activity of the tailings without active excitation treatment is quite low. The improvement of mechanical properties may be due to the higher strength of IOT itself as a skeleton.

3.3.3. Microstructural Tests

NMR Test

The previously prepared test specimens were cured under the same conditions for 7 d and 28 d, and then subjected to nuclear magnetic resonance (NMR) tests. The results for overall porosity are shown in Table 6. At different curing ages, the incorporation of IOT effectively reduced the porosity of the IOTC specimens. In specimens with the same IOT content, the change in age had less effect on the porosity.

Table 6. NMR analysis results of porosity.

Group		Porosity (%)
7 d	SCM	11.40
	SIM1	10.87
	SIM2	8.99
28 d	WCM	10.94
	WIM1	9.42
	WIM2	8.94

The T_2 spectral area is positively correlated with the amount of liquid contained in the mortar pores, which means that the variations in the T_2 spectral distribution can reflect the changes in pore volume. In the T_2 spectral distribution graph, the transverse X-axis indicates the relaxation time, which is proportional to the pore size: the longer the relaxation time, the larger the pore size. The longitudinal Y-axis indicates the pore signal intensity: the stronger the signal, the greater the number of pores [42,43]. The T_2 spectrum of each specimen is shown in Figure 12.

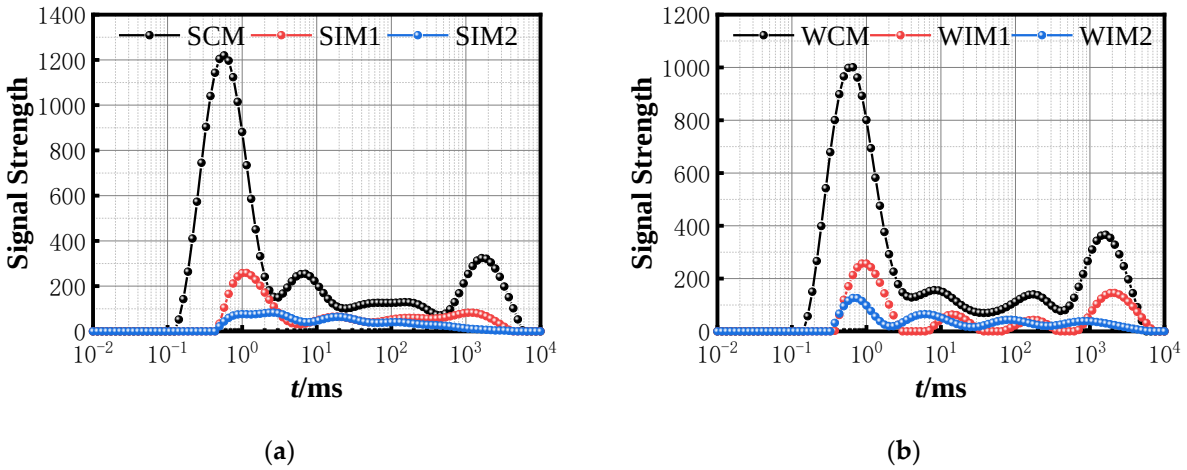

Figure 12. T_2 spectrum of different specimens: (**a**) 7 d; (**b**) 28 d.

The T_2 peaks of each mortar specimen in Figure 12 all have four peaks, including one main peak and three subpeaks. The positions of the main peaks are all at the short relaxation time—that is, the main peak is for the small pore size and the three subpeaks are for the large pore size. The areas of the main peaks are shown in Figure 13. The peak values and total areas of the main peak are both larger than those of the subpeaks, indicating that the volume and number of small pores are the largest and the volume and number of large pores are smaller in each mortar specimen. In addition, the area of each peak of the T_2

spectrum gradually decreases with the increase of IOT incorporation, demonstrating that the total number of internal pores as well as porosity are gradually decreasing, which is consistent with the mechanical test results.

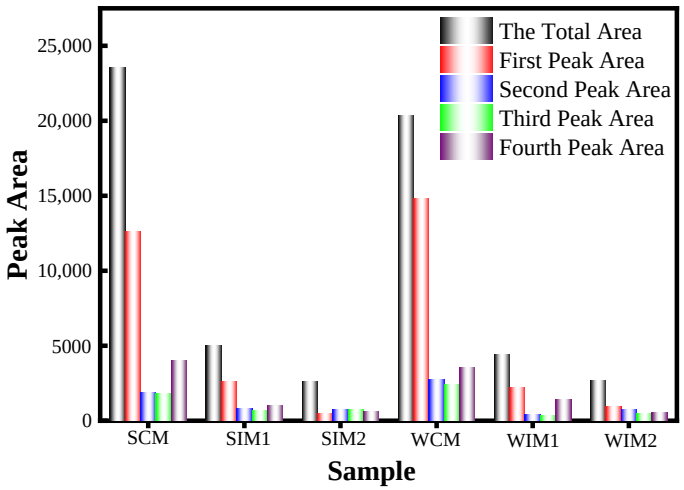

Figure 13. Peak areas of the sample.

The "chemical effect" of IOT on pores can be indirectly assessed from the perspective of curing age. Figure 14 shows the T_2 spectra of the mortar specimens with the same IOT substitution rate at different ages.

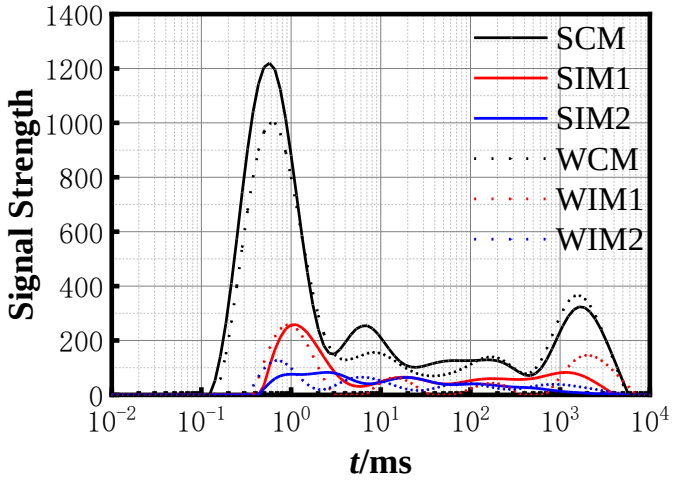

Figure 14. Distribution of T_2 spectra of specimens with ages of the same sand rate generation.

Using the CM group without tailings as the reference group, with the prolongation of the curing age, the level of microporosity decreases in the CM group, and the number of medium and large pores does not change much. The IM1 group with 25% sand substitution rate shows a little change in microporosity, but the number of medium-sized pores decreases, and large-sized pores increase. The IM2 group with 50% sand substitution rate shows an increase both in the microporosity and number of large pores, while the number of medium-sized pores decreases. However, the magnitude of the changes in these two IOTC groups is much smaller than in the CM reference group.

Combined with the aforementioned results, in general, the variation of the internal pores of the specimens according to curing age is small, and the effect of the internal pores of the test group by age is much less than the effect of the IOT substitution.

To further analyze the effect of IOT incorporation on the pore size and distribution of the internal pores, the T_2 spectrum distribution map was transformed into a pore

size distribution map. According to the NMR principle, the relationship between the chirality time and the internal pores of the material can be simplified and expressed as follows [44,45]:

$$\frac{1}{T_2} = \rho \frac{S}{V} \tag{3}$$

where ρ is the relaxation coefficient of the material, S is the surface area of the pores, and V is the volume of the pores, assuming that the pores in the mortar specimen are ideal spheres. Taking the chirality strength of the mortar as ρ = 12 μm/s according to the literature [46], the conversion relation between the pore radius and T_2 can be obtained:

$$\mathrm{R} = 36\ T_2 \tag{4}$$

The pore volume occupied by pores corresponding to a certain pore size is [47]:

$$V_i = \frac{A_i}{\sum A} \frac{m_s - m_d}{\rho_w} \tag{5}$$

where A_i is the NMR signal intensity corresponding to a certain T_2 value, m_s is the mass of saturated specimen, m_d is the mass of dried specimen, and ρ_w is the density of water, which is taken as 1.0 g/cm^3.

According to Equations (3)–(5), the T_2 spectral curve of mortar specimens can be converted into a pore size distribution curve, as shown in Figure 15. The specific pore size distribution inside the specimen was obtained based on the pore size distribution curve, which is shown in Table 7. From Figure 15 and Table 7, it can be seen that, at the early age, the admixture of tailings makes the minimum pore size inside the mortar gradually larger, the maximum pore size smaller, and the pore size distribution more concentrated. The specimens at 28 d also show the same trends.

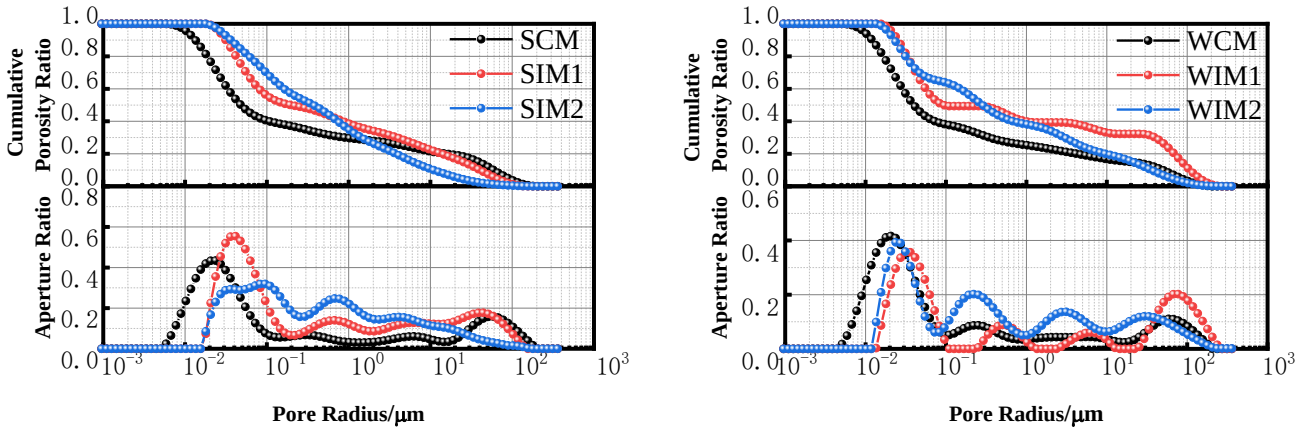

Figure 15. Specimen pore size distribution curve: (**a**) 7 d; (**b**) 28 d.

Table 7. Aperture distribution (unit: μm).

Group		The Pore Size of First Peak	The Pore Size of Second Peak	The Pore Size of Third Peak	The Pore Size of Fourth Peak	MIN	MAX
7 d	SCM	0.01–0.05	0.15–0.78	2.72–12.64	25.40–135.54	0.01	206.01
	SIM1	0.02–0.09	0.34–1.36	2.72–10.99	22.10–89.17	0.02	179.17
	SIM2	0.02–0.05	0.06–0.17	0.34–1.36	2.37–9.56	0.02	155.84
28 d	WCM	0.01–0.04	0.11–0.59	1.79–8.31	29.20–135.54	0.005	272.33
	WIM1	0.02–0.01	0.29–0.89	3.60–10.99	38.60–155.83	0.01	236.86
	WIM2	0.02–0.04	0.13–0.44	1.56–6.29	16.71–67.46	0.01	236.86

The different types of pore sizes inside the mortar can be divided into [48]: gelling pores, R < 10^{-2} μm, with a relaxation time T_2 < 1 ms; capillary pores, 10^{-2} μm < R < 5 μm, with a relaxation time 1 ms < T_2 < 500 ms; and noncapillary pores, R > 5 μm, with a relaxation time T_2 > 500 ms. Figure 16 shows the distribution of pore size types inside the mortar specimens. Gelling holes were found only in the CM group, indicating that micronized powder filled the gelling pores, resulting in a significant decrease in the percentage of small-sized pores, while the percentage of noncapillary pores decreased with curing age. After the addition of IOT, the gelatified pores disappeared, and the percentage of noncapillary pores increased with curing age for different IOT substitution samples, while the percentage of capillary pores gradually decreased. For different IOT substitution samples of the same age, the percentage of noncapillary pores first increased and then decreased with the increase of IOT substitution. This is related to both curing age and the adding of IOT.

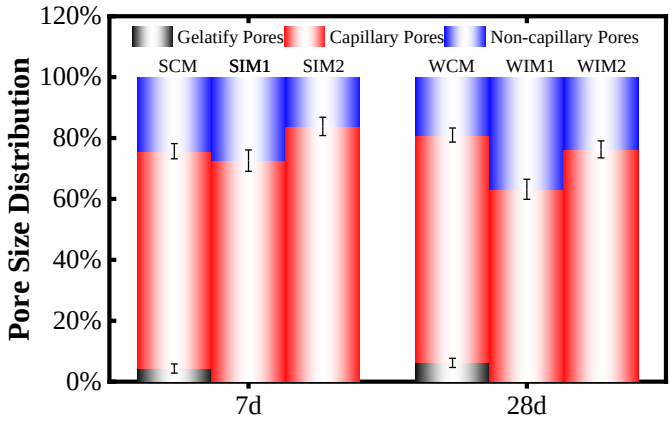

Figure 16. Type distribution of pore size in samples.

The above results show that the incorporation of IOT reduces the number and volume of pores inside the specimens, and the specimens have better mechanical properties, mainly due to the filling effect of IOT. In addition, the incorporation of tailings also makes the pore size distribution more concentrated.

SEM-EDS Test

Figure 17 shows the internal microscopic morphology and energy spectrum of the specimens at 7 d and 28 d of curing age. P1 to P6 in the figure are the points presented by EDS spectra.

From Figure 17a–c, it can be seen that all the mortar specimens of have richer hydration products at 7 d, with a large number of stacked or lumpy $Ca(OH)_2$ and flocculent C-S-H gels between the lumpy $Ca(OH)_2$. Similarly, in Figure 17d–f, the hydration products at 28 d are also lumpy $Ca(OH)_2$ and flocculent C-S-H gels, and there were no more obvious differences in the quantities and types of hydration products among the samples.

The EDS results on the right side of each subplot show the elemental composition (Wt% and At% omic) of the left side plot. O, Ca, Si, Al, and Na are also presented in the six subplots. At the same curing age, with the increase in IOT substitution, the mass proportion of Si element in the EDS results decreases and the mass proportion of Al element increases, which may because of the less content of SiO_2 in IOT than that of ISO sand.

The micromorphology results show that the incorporation of IOT has limited influences on the hydration products. The change of internal elemental content may be caused by the "physical effect" of IOT, which is consistent with the ICP-OES results and XRD results.

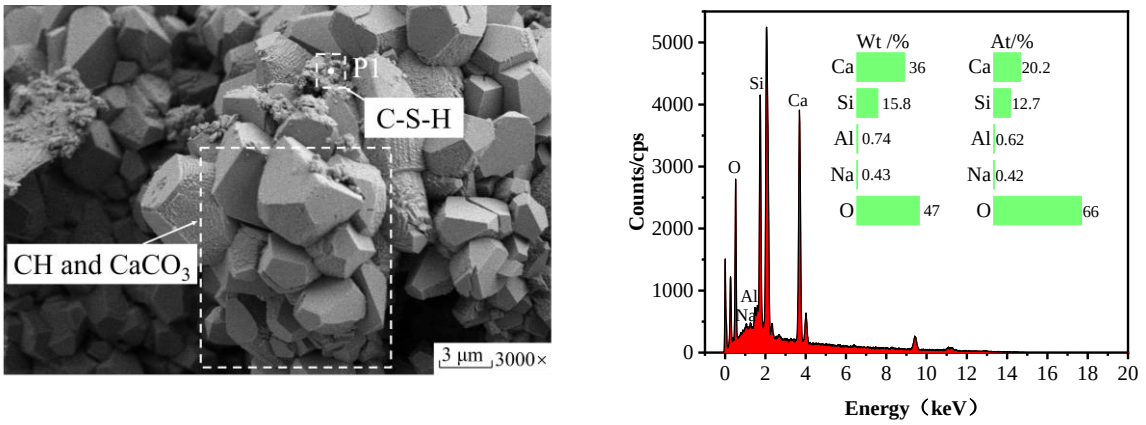

(**a**) SCM

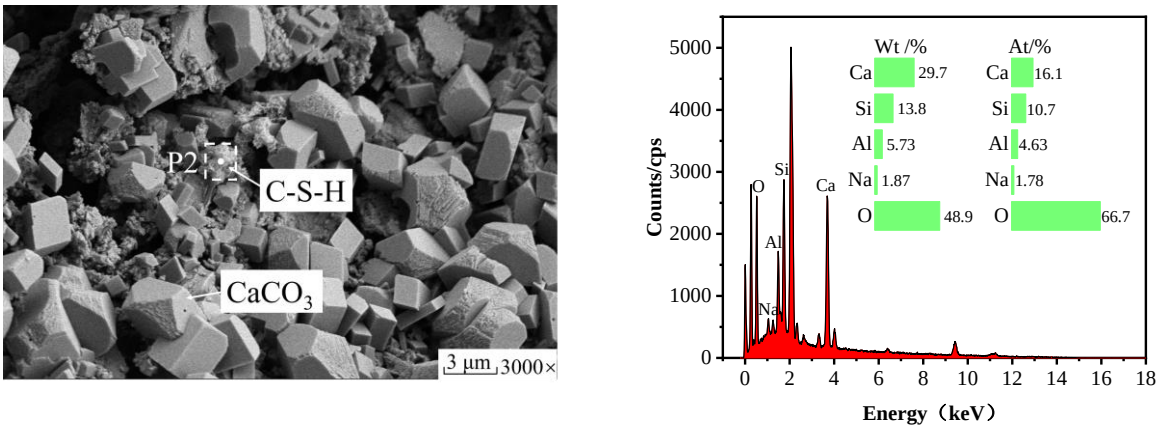

(**b**) SIM1

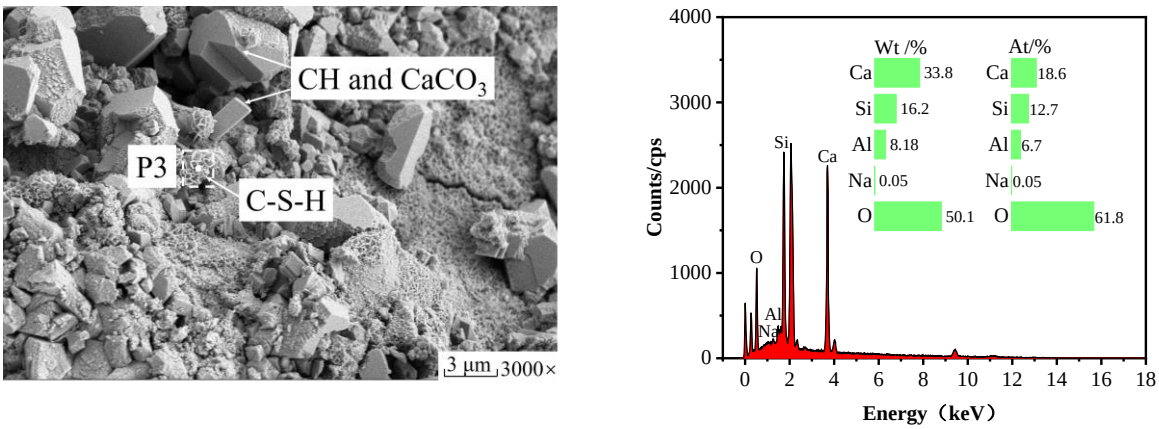

(**c**) SIM2

Figure 17. *Cont.*

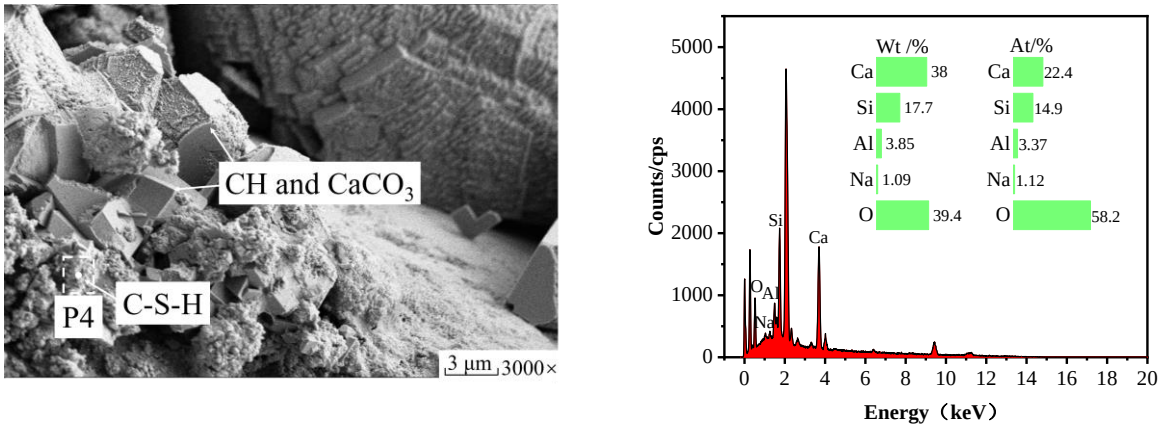

(**d**) WCM

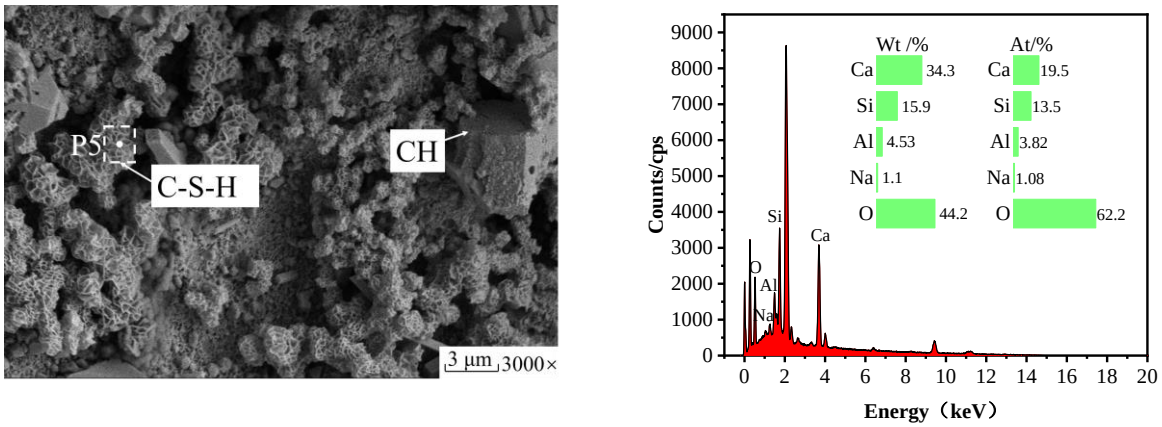

(**e**) WIM1

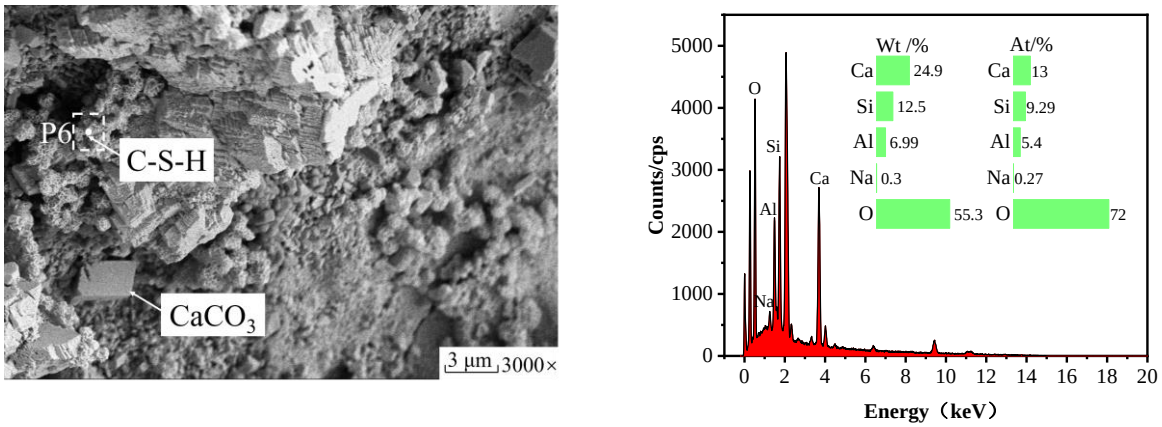

(**f**) WIM2

Figure 17. SEM-EDS results of different specimens: (**a**) SCM; (**b**) SIM1; (**c**) SIM2; (**d**) WCM; (**e**) WIM1; (**f**) WIM2.

4. Conclusions

The effects of IOT incorporation on the mechanical properties and microstructure of cement mortars were investigated by uniaxial compressive test, uniaxial tensile test, and fracture test, ICP-OES, XRD, NMR, and SEM-EDS tests, and the effects of curing time were considered. The following conclusions were reached:

(1) The IOT sand belongs to the category of fine sand and can partly substitute river sand to produce cement mortar and concrete.
(2) In the 0–50% IOT substitution rate tested in this paper, though the early strength was not enhanced by IOT incorporation, the potential strength improvement was obvious, especially for curing ages of 28 d and 120 d.
(3) Though limited chemical effect was found by adding IOT, in comparison with ISO sand mortar, the pore size distribution was changed for IOTC, which corresponds to its mechanical improvement.
(4) It is feasible to use IOT as construction material, with benefits both for solid waste utilization and engineering construction cost reduction.

Author Contributions: Conceptualization, W.R. and A.Z.; methodology, W.R. and J.L.; tests and data curation, J.L. and S.L.; resources, H.L. and A.Z.; writing—original draft preparation, J.L. and W.R.; writing—review and editing, W.R. and J.T.; funding acquisition, A.Z. and H.L. All authors have read and agreed to the published version of the manuscript.

Funding: This research is supported by the National Natural Science Foundation of China (51978572).

Institutional Review Board Statement: Not applicable.

Informed Consent Statement: Not applicable.

Data Availability Statement: Not applicable.

Conflicts of Interest: The authors declare no conflict of interest.

Abbreviations

List of symbols:

μ_f	Fineness modulus
f_c	Uniaxial compressive strength (unit: MPa)
f_t	Uniaxial tensile strength (unit: MPa)
P_{max}	Ultimate fracture load (unit: N)
a_c	Uniaxial compressive strength activity index (unit: %)
a_t	Uniaxial tensile strength activity index (unit: %)
a_f	Ultimate fracture load activity index (unit: %)
β_c	Coefficient of development of uniaxial compressive strength (unit: %)
β_t	Coefficient of development of uniaxial tensile strength (unit: %)
β_f	Coefficient of development of ultimate fracture load (unit: %)
T_2	Relaxation time (unit: ms)
ρ	Relaxation strength (unit: μm/s)
S	Pore surface area (unit: mm)
V	Pore volume (unit: mm^3)
R	Pore body radius (unit: μm)
V_i	The percentage of pore volume occupied by pores of a given pore size (unit: %)
A_i	NMR signal intensity corresponding to a certain T_2 value
m_s, m_d	The quality of saturated sample, the quality of dried samples, respectively (unit: g)
ρ_w	The density of water (unit: g/cm^3)

References

1. Gou, M.; Zhou, L.; Then, N.W.Y. Utilization of tailings in cement and concrete: A review. *Sci. Eng. Compos. Mater.* **2019**, *26*, 449–464. [CrossRef]
2. Gayana, B.C.; Chandar, K.R. Sustainable Use of Mine Waste and Tailings with Suitable Admixture as Aggregates in Concrete Pavements—A Review. *Adv. Concr. Constr.* **2018**, *6*, 221–243. [CrossRef]
3. Han, F.; Song, S.; Liu, J.; Huang, S. Properties of steam-cured precast concrete containing iron tailing powder. *Powder Technol.* **2019**, *345*, 292–299. [CrossRef]
4. Ruidong, W.; Yu, S.; Juanhong, L.; Linian, C.; Guangtian, Z.; Yueyue, Z. Effect of Iron Tailings and Slag Powders on Workability and Mechanical Properties of Concrete. *Front. Mater.* **2021**, *8*, 723119. [CrossRef]
5. Zhao, J.; Ni, K.; Su, Y.; Shi, Y. An evaluation of iron ore tailings characteristics and iron ore tailings concrete properties. *Constr. Build. Mater.* **2021**, *286*, 122968. [CrossRef]
6. Cheng, Y.; Huang, F.; Li, W.; Liu, R.; Li, G.; Wei, J. Test research on the effects of mechanochemically activated iron tailings on the compressive strength of concrete. *Constr. Build. Mater.* **2016**, *118*, 164–170. [CrossRef]
7. Gao, S.; Cui, X.; Zhang, S. Utilization of Molybdenum Tailings in Concrete Manufacturing: A Review. *Appl. Sci.* **2019**, *10*, 138. [CrossRef]
8. Li, T.; Wang, S.; Xu, F.; Meng, X.; Li, B.; Zhan, M. Study of the basic mechanical properties and degradation mechanism of recycled concrete with tailings before and after carbonation. *J. Clean. Prod.* **2020**, *259*, 120923. [CrossRef]
9. Jiang, Y.; Wang, H.; Chen, Y.; Ruan, M.; Li, W. Preparations of composite concretes using iron ore tailings as fine aggregates and their mechanical behavior. *Mater. Teh.* **2019**, *53*, 467–472. [CrossRef]
10. Arbili, M.M.; Alqurashi, M.; Majdi, A.; Ahmad, J.; Deifalla, A.F. Concrete Made with Iron Ore Tailings as a Fine Aggregate: A Step towards Sustainable Concrete. *Materials* **2022**, *15*, 6236. [CrossRef]
11. Chen, Z.; Chen, S.; Zhou, Y.; Zhang, C.; Meng, T.; Jiang, S.; Liu, L.; Hu, G. Effect of incorporation of rice husk ash and iron ore tailings on properties of concrete. *Constr. Build. Mater.* **2022**, *338*, 127584. [CrossRef]
12. Huang, X.; Ranade, R.; Ni, W.; Li, V.C. Development of green engineered cementitious composites using iron ore tailings as aggregates. *Constr. Build. Mater.* **2013**, *44*, 757–764. [CrossRef]
13. Siddique, S.; Jang, J.G. Assessment of molybdenum mine tailings as filler in cement mortar. *J. Build. Eng.* **2020**, *31*, 101322. [CrossRef]
14. Wu, R.; Liu, J. Experimental Study on the Concrete with Compound Admixture of Iron Tailings and Slag Powder under Low Cement Clinker System. *Adv. Mater. Sci. Eng.* **2018**, *2018*, 9816923. [CrossRef]
15. Zhang, Y.; Yang, D.; Gu, X.; Chen, H.; Li, Z. Application of Iron Tailings-Based Composite Supplementary Cementitious Materials (SCMs) in Green Concrete. *Materials* **2022**, *15*, 3866. [CrossRef]
16. Fontes, W.C.; Mendes, J.C.; Da Silva, S.N.; Peixoto, R.A.F. Mortars for laying and coating produced with iron ore tailings from tailing dams. *Constr. Build. Mater.* **2016**, *112*, 988–995. [CrossRef]
17. Zhao, Y.; Gu, X.; Qiu, J.; Zhang, W.; Li, X. Study on the Utilization of Iron Tailings in Ultra-High-Performance Concrete: Fresh Properties and Compressive Behaviors. *Materials* **2021**, *14*, 4807. [CrossRef] [PubMed]
18. Yang, L.; Xu, F. Experimental Study on the Effect of Fine Powder in Iron Tailings on the Durability of Ordinary Dry Mixed Mortar. *Integr. Ferroelectr.* **2021**, *213*, 1–11. [CrossRef]
19. Borges, P.H.R.; Ramos, F.C.R.; Caetano, T.R.; Panzerra, T.H.; Santos, H. Reuse of iron ore tailings in the production of geopolymer mortars. *REM Int. Eng. J.* **2019**, *72*, 581–587. [CrossRef]
20. Cui, L.; Chen, P.; Wang, L.; Xu, Y.; Wang, H. Reutilizing Waste Iron Tailing Powders as Filler in Mortar to Realize Cement Reduction and Strength Enhancement. *Materials* **2022**, *15*, 541. [CrossRef]
21. *GB/T 17671-2021*; China Building Materials Academy. Method of Testing Cements-Determination of Strength. Standards Press of China: Beijing, China, 2021.
22. *SL/T 352-2020*; Ministry of Water Resources of the People's Republic of China. Test Code for Hydraulic Concrete. China Water&Power Press: Beijing, China, 2020.
23. Kuruppu, M.D.; Obara, Y.; Ayatollahi, M.R.; Chong, K.P.; Funatsu, T. ISRM-Suggested Method for Determining the Mode I Static Fracture Toughness Using Semi-Circular Bend Specimen. *Rock Mech. Rock Eng.* **2014**, *47*, 267–274. [CrossRef]
24. *GB/T 14684-2022*; State Administration for Market Regulation and Standardization Administration of the People's Republic of China. Sand for Construction. Standards Press of China: Beijing, China, 2022.
25. *GB/T 2419-2005*; State Administration for Market Regulation and Standardization Administration of the People's Republic of China. Test Method for Fluidity of Cement Mortar. Standards Press of China: Beijing, China, 2005.
26. *GB/T 50123-2019*; Ministry of Water Resources of the People's Republic of China. Standard for Soil Test Method China Planning Press: Beijing, China, 2019.
27. Wang, Y.; Gu, X.W.; Zhang, Y.N.; Yin, S.Q.; Xu, X.C.; Wang, Q. Analysis of Compressive Strength and Microstructure of Iron Tailings Sand Cement Mortar. *Metal Mine.* **2022**, *51*, 60–64. [CrossRef]
28. Song, J.; Wang, L.; Liu, S.; Zhu, J.; Ouyang, Y. Comparison Study of Hydration Characteristics Between Cements with 50% and 85% Slag. *Mater. Sci.* **2018**, *24*, 421–427. [CrossRef]
29. Papadakis, V.; Tsimas, S. Supplementary cementing materials in concrete: Part I: Efficiency and design. *Cem. Concr. Res.* **2002**, *32*, 1525–1532. [CrossRef]

30. Thomas, B.S.; Damare, A.; Gupta, R. Strength and durability characteristics of copper tailing concrete. *Constr. Build. Mater.* **2013**, *48*, 894–900. [CrossRef]
31. Cheng, Y.; Huang, F.; Qi, S.; Li, W.; Liu, R.; Li, G. Durability of concrete incorporated with siliceous iron tailings. *Constr. Build. Mater.* **2020**, *242*, 118147. [CrossRef]
32. Esmaeili, J.; Aslani, H.; Onuaguluchi, O. Reuse Potentials of Copper Mine Tailings in Mortar and Concrete Composites. *J. Mater. Civ. Eng.* **2020**, *32*, 04020084. [CrossRef]
33. Song, J.W.; Zhu, J.L.; Liu, F.H.; Feng, S.L. Influence of Copper Tailing Powder on the Compressive Strength and Microscopic Structure of Complex Binder. *J. Build. Mater.* **2019**, *22*, 846–852. [CrossRef]
34. Zhang, W.; Gu, X.; Qiu, J.; Liu, J.; Zhao, Y.; Li, X. Effects of iron ore tailings on the compressive strength and permeability of ultra-high performance concrete. *Constr. Build. Mater.* **2020**, *260*, 119917. [CrossRef]
35. Zhang, N.; Tang, B.; Liu, X. Cementitious activity of iron ore tailing and its utilization in cementitious materials, bricks and concrete. *Constr. Build. Mater.* **2021**, *288*, 123022. [CrossRef]
36. Maglad, A.M.; Zaid, O.; Arbili, M.M.; Ascensão, G.; Șerbănoiu, A.A.; Grădinaru, C.M.; García, R.M.; Qaidi, S.M.A.; Althoey, F.; de Prado-Gil, J. A Study on the Properties of Geopolymer Concrete Modified with Nano Graphene Oxide. *Buildings* **2022**, *12*, 1066. [CrossRef]
37. Malathy, R.; Sentilkumar, S.R.R.; Prakash, A.R.; Das, B.B.; Chung, I.-M.; Kim, S.-H.; Prabakaran, M. Use of Industrial Silica Sand as a Fine Aggregate in Concrete—An Explorative Study. *Buildings* **2022**, *12*, 1273. [CrossRef]
38. Churata, R.; Almirón, J.; Vargas, M.; Tupayachy-Quispe, D.; Torres-Almirón, J.; Ortiz-Valdivia, Y.; Velasco, F. Study of Geopolymer Composites Based on Volcanic Ash, Fly Ash, Pozzolan, Metakaolin and Mining Tailing. *Buildings* **2022**, *12*, 1118. [CrossRef]
39. Song, F.; Yu, Z.; Yang, F.; Lu, Y.; Liu, Y. Microstructure of amorphous aluminum hydroxide in belite-calcium sulfoaluminate cement. *Cem. Concr. Res.* **2015**, *71*, 1–6. [CrossRef]
40. Li, H.; Xu, C.; Dong, B.; Chen, Q.; Gu, L.; Yang, X. Enhanced performances of cement and powder silane based waterproof mortar modified by nucleation C-S-H seed. *Constr. Build. Mater.* **2020**, *246*, 118511. [CrossRef]
41. Justnes, H.; Skocek, J.; Østnor, T.A.; Engelsen, C.J.; Skjølsvold, O. Microstructural changes of hydrated cement blended with fly ash upon carbonation. *Cem. Concr. Res.* **2020**, *137*, 106192. [CrossRef]
42. Yi, Z.-L.; Sun, H.-H.; Li, C.; Sun, Y.-M.; Li, Y. Relationship between polymerization degree and cementitious activity of iron ore tailings. *Int. J. Miner. Met. Mater.* **2010**, *17*, 116–120. [CrossRef]
43. Peng, Y.; Liu, Y.; Zhan, B.; Xu, G. Preparation of autoclaved aerated concrete by using graphite tailings as an alternative silica source. *Constr. Build. Mater.* **2021**, *267*, 121792. [CrossRef]
44. Wu, C.; Yang, S.; Cai, J.; Zhang, Q.; Zhu, Y.; Zhang, K. Activated Microporous Carbon Derived from Almond Shells for High Energy Density Asymmetric Supercapacitors. *ACS Appl. Mater. Interfaces* **2016**, *8*, 15288–15296. [CrossRef] [PubMed]
45. Al-Qodah, Z.; Shawabkah, R. Production and characterization of granular activated carbon from activated sludge. *Braz. J. Chem. Eng.* **2009**, *26*, 127–136. [CrossRef]
46. Xue, S.; Meng, F.; Zhang, P.; Bao, J.; Wang, J.; Zhao, K. Influence of water re-curing on microstructure of heat-damaged cement mortar characterized by low-field NMR and MIP. *Constr. Build. Mater.* **2020**, *262*, 120532. [CrossRef]
47. Li, T.G.; Kong, L.W.; Wang, J.T.; Wang, F.H. Trimodal pore structure evolution characteristics and mechanical effects of expansive soil in seasonally frozen areas based on NMR test. *Rock Soil Mech.* **2021**, *42*, 2741–2754. [CrossRef]
48. Kumar, R.; Bhattacharjee, B. Study on some factors affecting the results in the use of MIP method in concrete research. *Cem. Concr. Res.* **2003**, *33*, 417–424. [CrossRef]